



Analysis of floating objects based on non-intrusive measuring methods and machine learning

Mateja Škerjanec^{a,*}, Klemen Kregar^b, Gašper Štebe^b, Gašper Rak^a

^a Chair of Fluid Mechanics, Faculty of Civil and Geodetic Engineering, University of Ljubljana, 1000 Ljubljana, Slovenia

^b Chair of Geodesy, Faculty of Civil and Geodetic Engineering, University of Ljubljana, 1000 Ljubljana, Slovenia

ARTICLE INFO

Keywords:

Floating objects
Laser scanning
Machine learning
Volume estimation

ABSTRACT

Floating objects in rivers and streams present a growing problem, not only as they may cause clogging of bridges and other hydraulic structures, and consequently floods, but also because they can have a diverse impact on river (and marine) ecosystems, either positive (in case of in-channel wood) or negative (in case of anthropogenic floating objects). To automatically identify different types of floating objects (i.e., wood pieces, EPS and XPS boards, and plastic and metal containers) and their volumes in an open channel, we propose a novel methodology based on non-intrusive measuring methods and machine learning. To this end, we tested the combination of an industrial 2D laser scanner, a high-speed camera, and an ultrasonic sensor. In the laboratory experiment, 36 samples were scanned separately, two to three times in a row, resulting in 77 raw LIDAR clouds and image sequences. Raw data were post-processed with custom-developed algorithms to determine the volumes of samples above the water surface and their intensity histograms. The latter were analyzed with the machine learning algorithm to distinguish between different material types of floating objects. For each of them, the material density was assigned. Based on the identified floating object's material type, pre-assigned density, and measured volume above the water surface, the sample volumes were calculated and compared with the actual ones determined before setting up the experiment. The results show that the proposed approach enables material recognition with accuracy higher than 90%. The average volume calculation error based on detected material type, assigned densities, and measured floating object's volume above the water surface is approx. 2%. The proposed methodology proved promising for automatic differentiation between different types of floating objects and remote measurement of their volume. To use the method in real-world applications (e.g., on bridges) for forecasting downstream quantities of floating objects, and consequently adjusting their management accordingly, additional measurements are needed, focusing on simultaneous scanning of multiple floating objects, under different flow conditions.

1. Introduction

Floating objects commonly found in rivers and streams consist of in-channel wood and anthropogenic floating objects. The latter refer to any persistent solid material disposed in the environment by human activities (e.g., plastic bottles and foam take-out containers), while in-channel wood results from natural processes. Bigger pieces, such as large wood or macro plastics, may induce significant obstructions along the river network, clogging hydraulic structures and bridges (e.g., Panici et al., 2020), which can damage instream infrastructure and can lead to an increase in the upstream water level, inducing floods (Ruiz-

Villanueva et al., 2016a). Thus, floating objects pose a great challenge to flood risk management (Gschnitzer et al., 2017).

Although in-channel floating objects, especially large wood, have been recognized to play an important role in river ecology, morphology, and hydraulics, a knowledge of their mobilization, transport, and deposition dynamics during high-magnitude flood events still remains very scarce, mostly because such events are difficult to monitor in-field due to considerable investments in terms of time and costs, but also because such activities may be potentially dangerous (Kramer and Wohl, 2015; Comiti et al., 2016; Ruiz-Villanueva et al., 2016a; Sanhueza et al., 2019; Wohl et al., 2019).

* Corresponding author.

E-mail addresses: mateja.skerjanec@fgg.uni-lj.si (M. Škerjanec), klemen.kregar@fgg.uni-lj.si (K. Kregar), gasper.stebe@fgg.uni-lj.si (G. Štebe), gasper.rak@fgg.uni-lj.si (G. Rak).

<https://doi.org/10.1016/j.geomorph.2022.108254>

Received 21 September 2021; Received in revised form 8 April 2022; Accepted 9 April 2022

Available online 12 April 2022

0169-555X/© 2022 The Authors. Published by Elsevier B.V. This is an open access article under the CC BY license (<http://creativecommons.org/licenses/by/4.0/>).

Consequently, different non-intrusive measuring methods (e.g., aerial photography and remote sensing) have been increasingly used in the past decade, both for measuring flow properties and complex hydraulic phenomena and for monitoring the dynamics of floating objects in rivers. Below, we mention some of the notable examples.

In terms of hydraulics, image processing techniques like (micro-) particle and bubble image velocimetry (e.g., [Kantoush et al., 2008](#); [Bung and Valero, 2016](#); [Fan et al., 2018](#)), optical flow (e.g., [Bung and Valero, 2016](#)) and computer-aided visualization methods (e.g., [Bizjan et al., 2014](#); [Müller et al., 2015](#)) have been applied to provide 2D and 3D velocity fields and detailed shear stress distribution. A combination of a high-speed camera and ultrasonic sensors has been used for the determination of dynamic free-water surface levels and for the investigation of air-water flows ([Zhang et al., 2018](#)). Additionally, laser scanning as a firmly established remote sensing technique has proved efficient in the acquisition of free-water surface topography of highly aerated flows. With its high spatial and temporal resolution, the method was successfully used to profile time-averaged free-water surface, calculate standard deviation, and estimate frequency spectra of free-water surface fluctuations of a hydraulic jump, flows on stepped spillways, and turbulent supercritical junction flow ([Montano and Felder, 2018](#); [Kramer et al., 2020](#); [Rak et al., 2020a,b](#)).

In the floating objects monitoring domain, non-intrusive methods have mainly been used for the large wood assessment in rivers causing wood jams. [MacVicar and Piégay \(2012\)](#) applied a video camera and a semi-manual logging algorithm to detect and measure wood passing the selected gauging station. Later on, Google Earth® satellite images were used for the identification of large wood across greater spatial scales ([Atha, 2013](#)) and to investigate its spatial distribution and volumes ([Ulloa et al., 2015](#)). Large wood jams and accumulations were also studied by using airborne Light Detection and Ranging (LIDAR) data sets ([Kasprak et al., 2012](#); [Abalharth et al., 2015](#); [Magnussen et al., 2018](#)), and by Structure from Motion (SfM) acquisition ([Sanhueza et al., 2019](#); [Spreitzer et al., 2019, 2020](#)). [Atha and Dietrich \(2016\)](#) used LIDAR data to identify and quantify single logs and log jams in rivers flowing through forested catchments. To detect large wood characteristics and its volumes in riverine environments, Terrestrial Laser Scanners (TLS) have also been applied ([Tonon et al., 2014](#); [Grigillo et al., 2015](#)). Recently, video monitoring, supported by automatic detection and characterization algorithms, has been proposed for wood mobility quantification and estimation of the size distribution of floating wood logs, which has also been tested in the field ([Ghaffarian et al., 2020a, 2021](#); [Zhang et al., 2021](#)). By applying post-processing and training the software algorithms, the method has provided reliable results with an error of about 6.5% for wood pieces number estimation and 13.5% for volume detection. However, the accuracy of the results depends significantly on the installation (position and inclination) and configuration (resolution) of a camera, as well as on the light and flow conditions (i.e., light reflection and water waves).

Although plastic floating objects are considered one of the most important global issues, especially along the coasts and in the open seas ([Hu, 2021](#)), research regarding the identification and transport of macro plastics in contributing rivers is limited.

To automatically differentiate between different floating object types commonly found in river channels and remotely measure their volume, we propose a combination of non-intrusive measuring methods (i.e., industrial 2D laser scanner, high-speed camera, and an ultrasonic sensor for free-water-surface measurements) and machine learning.

Machine learning is a field of artificial intelligence used to find complex patterns in data sets, thus allowing in-depth analyses of the data. Although originating from computer science, it has been gaining attention in other fields (also hydrology and hydraulics) due to its potential in discovering more accurate and efficient prediction models ([Mosavi et al., 2018](#); [Khosravi et al., 2020, 2021](#)).

To the best of our knowledge, no similar system has been applied for monitoring the type, shape, and volume of floating objects in rivers and

streams. The present work aims to answer the following research questions: (a) Can the combination of the 2D laser scanner, high-speed camera, and ultrasonic sensor be applied to identify the type and volume of floating objects? (b) What is the precision achieved with this approach in obtaining the dimensions (shape and volume) of a single floating object? (c) What are the limitations and advantages of this approach compared to the other methods for floating objects analysis? (d) What are the next steps needed to implement the proposed setup in real-world applications?

The paper is organized as follows. [Section 2](#) gives an overview of the experimental setup and the measuring methods applied. The results on material recognition and volume estimation of a single floating object sample are presented in [Section 3](#). [Section 4](#) introduces a thorough discussion on identified material misclassifications and volume errors, recommendations for practical application, and comparison with the other methods, followed by the conclusions in [Section 5](#).

2. Materials and methods

2.1. Floating object samples

We selected 36 samples of floating objects of different materials, densities, shapes, and sizes ([Fig. 1](#)). They were divided into three groups: a) wood (timber), b) empty plastic and metal packaging, and c) products made from the expanded and extruded polystyrene foam (EPS and XPS).

As for timber samples, 16 cylinders and rectangular cuboids of different dimensions made from coniferous wood were tested. Diameters of cylindrical samples were in the range between 45 mm and 139 mm, while widths and heights of rectangular cuboids were in the ranges from 44 mm to 160 mm, and 24 mm to 140 mm, respectively. Plastic and metal samples presented a selection of packaging products, i.e., bottles, containers, and jars of irregular (complex) shapes. They were all empty and sealed. EPS and XPS foam samples were rectangular cuboids of different dimensions. The width and height of the samples were ranging from 65 mm to 220 mm, and 50 mm to 57 mm, respectively, while their length varied between 185 mm and 339 mm.

Actual volumes of regular-shape samples (i.e., cylinders and cuboids) were calculated based on their dimensions, while the volumes of more complex shapes (i.e., plastic and metal containers) were determined by either weighing empty and full samples or measuring their dimensions. When assessing the effectiveness of the proposed method, the actual volumes were compared with the ones calculated based on the measurements and the assigned densities. The volume calculation procedure is presented in [Section 2.5](#).

2.2. Experimental set-up

Experiments were conducted in a straight rectangular flume, 6 m long, 0.5 m wide, and 0.5 m high ([Fig. 2](#)). To reduce hydraulic roughness and its effect on flow conditions and enable visual inspection of flow and floating objects, all walls and the bottom of the channel were constructed from glass plates with a minimum number of joints. Measurements were performed in a subcritical, steady-uniform flow regime. The discharge rate was 17 l/s at a water depth of 0.21 m, flow velocity 0.16 m/s, Reynolds number of $3.3 \cdot 10^4$, and a Froude number of 0.11. Flow conditions remained constant during the whole experiment.

The desired discharge was provided from a constant hydraulic head reservoir filled with tap water, through a pipeline equipped with a valve and a flow meter, and a vessel with an adjustable height of the opening. Water outflow from the model was over the sharp-crested rectangular weir.

The measuring equipment consisted of four main components: a laser scanner, a high-speed camera, an ultrasonic water level sensor, and a connecting mechanism, to which the scanner and the camera were firmly attached ([Figs. 2 and 3](#)). The above-mentioned measuring devices were mounted on a frame structure equipped with rigid metal rails and



Fig. 1. Samples used in the experiment. The numbers indicate unique labels of individual samples (i.e., sample IDs).

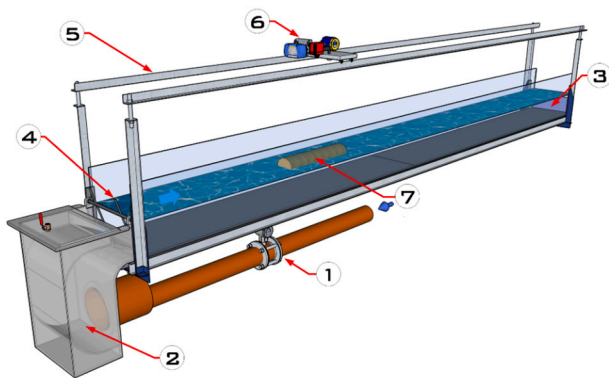


Fig. 2. Experimental setup: 1 – pipeline system equipped with a valve and a flowmeter; 2 – pressure vessel with adjustable height of the opening; 3 – free outflow over fixed weir; 4 – channel; 5 – rails with connecting mechanism for mounting and precise positioning of measuring devices; 6 – measuring equipment; 7 – floating object.

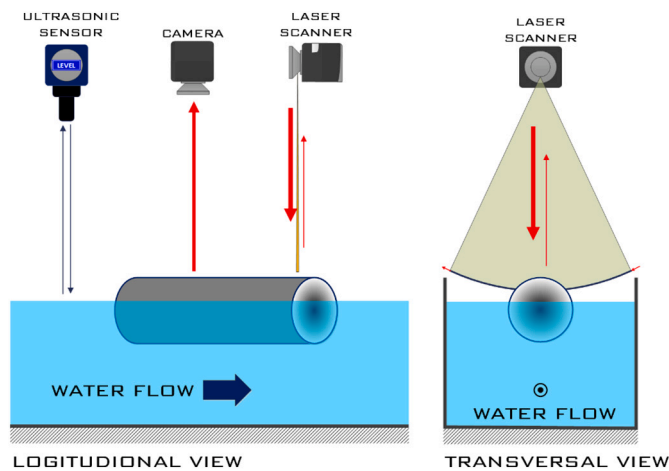


Fig. 3. Measuring devices, i.e., laser scanner, ultrasonic water level sensor and high-speed camera.

were positioned perpendicularly to and 1.2 m above the bottom of the channel.

Each sample was scanned separately, two to three times in a row. Samples passed the measuring area at various angles with respect to the longitudinal axis of the channel. Thus, each measurement (i.e., case) was attributed with orientation - either longitudinal, transverse, oblique or rotating.

Cases including samples with their long axis parallel or perpendicular to the longitudinal axis of the channel were attributed longitudinal or transverse orientation, respectively. If the sample's orientation deviated significantly from the longitudinal and transverse direction, oblique orientation was assigned. Since water flow in natural rivers is rarely uniform across a channel and as unevenly distributed velocities can cause whirls, the rotation of samples around the vertical axis was applied to analyze its effect on the accuracy of measurement. These cases were assigned the rotating orientation. Since sample 34 had a circular upper surface and a slightly conical form in the vertical direction, orientation was assigned up when its wider part was above the water surface and down when its wider part was immersed. Some samples of asymmetrical cross-sections also exhibited transversal tilt. However, this effect was not additionally marked.

2.2.1. Laser scanner

A commercially available laser scanner equipped with SICK 2D LIDAR sensor LMS4121R-13000 was used, which allows for high temporal and spatial resolution measurements. According to its technical data, the systematic and statistical measurement uncertainties are ± 1 mm and ± 1.5 mm, respectively.

The device operates at the visible red light with a wavelength of 660 nm, a line scanning frequency of 600 Hz, and an angular resolution of 0.0833° . The angular range of the device is 70° . In total, 504,000 distance measurements were performed per second (i.e., 600 profiles per second $\times 70^\circ$ field of measurement $\times 12$ measurements per single degree). Each scan line was composed of 840 measurement points.

For each emitted laser beam and received echo, reflected from the measured surface, the LIDAR sensor records a distance to the surface, angle, and remission data (i.e., the intensity of a returned signal, given as a value between 0 and 255 or as a percentage of emitted energy). The returned signal is always smaller than the emitted one and depends on the properties of the measured surface (e.g., on its material and structure), angle of incident, reflections on the surfaces smaller than the laser beam footprint (i.e., 1 mm), and energy dissipation of a signal traveling through water.

2.2.2. Ultrasonic sensor

Previous research has shown that the laser scanner measurements of clear, still tap water surfaces are hindered by beam penetration through the water and its reflection from the water surface. Since the laser beam is specularly reflected off the water surface, the received signal reaches the LIDAR sensor only at the null incident angle or very close to 0° (Rak et al., 2017). As the water surface of the applied subcritical flow is relatively smooth and flat, the laser scanner measurements directly below the device could provide water levels. However, due to significant measurement noise and uncertainty, the water level was acquired using the Endress + Hauser's Ultrasonic sensor Prosonic FMU40-ARB2A2 and

was controlled by a point gauge. The water level was measured with a precision of ± 0.1 mm.

2.2.3. High-speed camera

Detection of an object's shape and volume using a high-resolution 2D laser scanner requires information on its velocity relative to the laser sheet. For the velocity field determination, a high-speed Casio EX-F1 camera with an image acquisition frequency of 300 fps was used. The camera was positioned next to the laser scanner and was oriented perpendicular to the water surface and the flume bottom (Fig. 3).

The proposed method requires appropriate illumination and seeding. As the object's velocity is roughly related to water velocity (Ghaffarian et al., 2020b), the samples served as tracers. Thus, no additional seeding was needed. As illumination, ordinary daylight was used. Image sequences were obtained for all the measurements, i.e., 77 passes of various floating samples were recorded.

2.3. Data post-processing

Each scan line resulted in a row of 840 measured distances with corresponding intensity values. Obtained raw (textual) data were transmitted to the computer through a custom-made user interface written in Python and performed using the Ethernet connection.

The distance data obtained during each experiment is static and can be treated as point cloud data. The point cloud obtained from the measurements refers to the coordinate system presented in Fig. 4. Coordinate system origin is translated vertically from the scanner center to the water surface level. Z-axis is pointing upwards, Y-axis along the water flow, and X-axis transversely perpendicular to axes Y and Z.

The processing of distance data into a point cloud starts by decomposing each scan line of distances into vertical and horizontal components according to the vertical angle of a laser beam. Angular values in the scan line span from 55° to 125° with respect to the horizon, with a step of $5'$ (i.e., $5/60^\circ$). The horizontal component of the distance is referred to as the X coordinate and the vertical component as the Z coordinate. Values of the Y coordinate depend on the velocity of a floating object and water flow. Given the frequency of laser scanner measurements and water flow velocity, all points in a scan line are assigned the same value of Y coordinate according to the consecutive number of a scan line.

The points falling outside the channel are removed by thresholding X coordinate values. The ones reflected from a calm water surface are highly dispersed (except at incidence angles close to 0° , where the total internal reflection appears; Rak et al., 2017). However, they can be

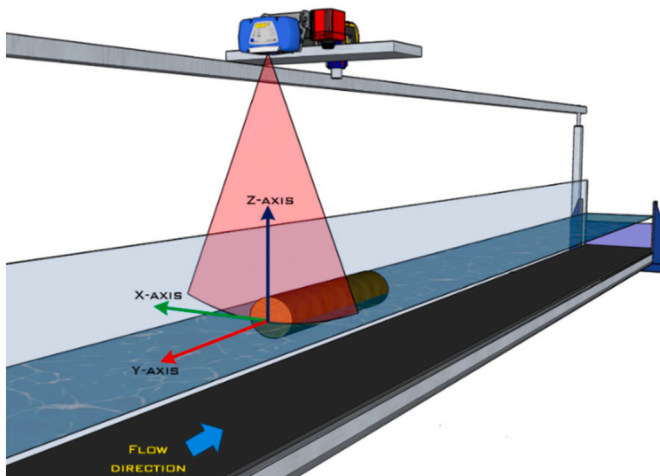


Fig. 4. Orientation of the point cloud coordinate system in the experimental setup.

efficiently removed by further filtration.

For fine-tuning, the *pcdenoise* function integrated into Matlab™ was used, which exploits the nearest neighbor filtering method, i.e., all points lacking a sufficient number of neighbors in a given neighborhood are removed from the cloud. At first, 100 neighbors inside a smaller area were required, followed by 20 neighbors inside a five times larger area. All the outliers have to be removed as they can severely affect the final results.

Next, a regular square grid (mesh) was built over the remaining points of the point cloud. To this end, a *griddata* interpolation function integrated into Matlab™ was applied, using linear interpolation to determine the values in a regular grid according to the position of points in the point cloud. A cell size of 5 mm was selected.

Based on regular square grid data, the volume of the floating sample part above the water surface was calculated by multiplying each cell height by the area of the cell (i.e., $5 \times 5 \text{ mm} = 25 \text{ mm}^2$) and by summing all partial (cell) volumes.

For image sequences post-processing obtained by a high-speed camera, the computer-aided visualization method was applied based on the advection-diffusion equation, integrated into the ADMflow software, developed by the University of Ljubljana, Faculty of Mechanical Engineering, and by the Abelium company (Bajcar et al., 2009). The ADMflow has been successfully used for measuring the velocity fields of free surface flows under various conditions (Müller et al., 2015; Novak et al., 2017).

2.4. Material recognition based on machine learning

Besides the measured distances, the laser scanner also records intensities of reflected laser beams which can be plotted as histograms. We decided to investigate these histograms and see whether we could identify patterns that would point to a particular material, thus allowing the automatic detection of a floating object material.

Histograms obtained for each case were vectorized, i.e., to each intensity interval (from 0–10 to 140–150), a percentage of recorded reflections was assigned. The resulting 77 vectors were analyzed with one of the most popular algorithms for pattern recognition, i.e., the IBk classifier incorporated into WEKA software (Aha et al., 1991).

IBk or a *k*-nearest neighbor algorithm is a non-parametric classification method. Its input consists of the *k* closest training examples in the data set for which the correct classification is known, while its output is a class membership. An object is assigned to the class most common among its *k*-nearest neighbors, where *k* is a positive (typically small) integer. If *k* = 1, then the object is assigned to the class of a single nearest neighbor (see Fig. 5).

The classification quality can be assessed through the 10-fold cross-

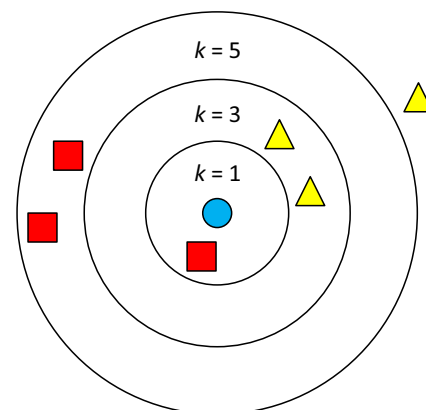


Fig. 5. A hypothetical example of IBk classification. The test sample (circle) can be classified as a square or triangle. If *k* = 1 or *k* = 5, it is assigned to squares, and if *k* = 3 to triangles.

validation. To this end, the whole dataset is divided into ten subsets. Nine subsets are used for training and one for testing. The same procedure is repeated ten times, each time with a different sub-set used for testing. The accuracy of each evaluation is computed based on comparing the actual vs. predicted class value. In our case, the class value represents the floating object material type. The final accuracy is the average accuracy of all ten evaluations.

2.5. Calculation of the sample volume

As the laser scanner can only detect a part of the floating sample above the water surface, a relationship between the measured volume above the water surface (V_{above}) and the entire sample volume (V) is needed. It can be derived from Archimedes' principle, which states that any object, wholly or partially immersed in a fluid, is buoyed up by force equal to the weight of the fluid displaced by the object (w_{fl}). Thus, buoyancy force (F_B) can be written as:

$$F_B = w_{fl} = m_{fl} \cdot g = \rho_{fl} \cdot V_{fl} \cdot g = \rho_{fl} \cdot V_{sub} \cdot g \quad (1)$$

where m_{fl} is the mass of the displaced fluid, g is gravitational acceleration, ρ_{fl} is the density of the displaced fluid, and V_{fl} is its volume, which is equal to the submerged volume of an object (V_{sub}). The weight force of an object (F_g) is termed as:

$$F_g = m \cdot g = \rho \cdot V \cdot g \quad (2)$$

where m , ρ , and V are the mass, density, and volume of the object, respectively. For an object to float, the F_g must be balanced with the F_B :

$$F_B = F_g \rightarrow \rho_{fl} \cdot V_{sub} \cdot g = \rho \cdot V \cdot g \quad (3)$$

Based on Eq. (3), the quantitative expression for the fraction submerged can be derived:

$$\frac{V_{sub}}{V} = \frac{\rho}{\rho_{fl}} \quad (4)$$

By replacing V_{sub} with $V - V_{above}$ and ρ_{fl} with ρ_{H2O} (which stands for water density), we get the following equation:

$$\frac{V - V_{above}}{V} = \frac{\rho}{\rho_{H2O}} \rightarrow V = \frac{V_{above} \cdot \rho_{H2O}}{\rho_{H2O} - \rho} \quad (5)$$

Now, we can express the object (floating sample) volume as:

$$V = \frac{V_{above} \cdot \rho_{H2O}}{\rho_{H2O} - \rho} \quad (6)$$

We can see that the floating object volume estimation also depends on its density, which is material-dependent. Although the tested samples' densities could be calculated according to the actual dimensions and weights, they were assigned based on detected material type to lay the foundation for real-world applications in which the densities are not provided and have to be somehow estimated. For samples classified as wood, we selected a density value of 580 kg/m³, which falls within the range of 660 ± 200 kg/m³ for instream wood provided by Ruiz-Villanueva et al. (2016b), considering broad-leaved trees species mostly which have higher densities than coniferous wood used in our experiment. Our samples were made of relatively fresh wood and were not completely soaked. For EPS and XPS samples, densities were assigned according to the average material specification provided by different manufacturers of EPS and XPS insulation boards, i.e., 10 kg/m³ and 30 kg/m³, respectively. In real-world applications, it is not possible to identify whether a floating packaging object (either metal or plastic) is empty or at least partially full. The only fact is that a filled packaging sample would not float on the water surface. Assuming that the most waste packaging is (almost) empty and that the type/volume of its content cannot be defined, the average densities of tested empty bottles, containers, and jars of irregular (complex) shapes were used, separately

for metal and plastic products. Thus, the density value of 55 kg/m³ was assigned to samples classified as plastic and 170 kg/m³ to samples classified as metal.

3. Results

3.1. Material recognition

For each of the 77 scanning cases, the histograms of the recorded intensities were obtained. First, the histograms were grouped according to the actual material type of the tested samples. The results are presented in Fig. 6, where the darker shade of grey tells us where the histograms overlap, thus indicating the most predominant shape of the histogram for a particular material type. Results show that the histograms of wooden samples can vary significantly, while the ones of EPS and XPS are more consistent. Plastic and metal samples have a similar intensity response, i.e., their histograms are of similar shapes.

Due to the large dispersion of histograms for wood samples, we decided to additionally divide them according to their shape, i.e., cylinder, cuboid, and cuboid-board. The results, presented in Fig. 7, indicate that the floating object's shape affects the intensity footprints.

Next, the obtained histograms were vectorized and analyzed with the WEKA software, namely with the IBk classifier, to see whether it is possible to automatically detect different floating object material types. According to the results, presented in Appendix A, the material type was correctly attributed to 70 (90.9%) samples. Only 7 (9.1%) samples were incorrectly classified, i.e., one wooden sample was incorrectly classified as EPS, two plastic samples as metal and one as XPS, one metal sample as wood and one as plastic, and one XPS sample as plastic.

3.2. Floating objects' volume calculation

By post-processing, the point clouds obtained with laser scanning (see an example in Fig. 8), we calculated the volumes of the floating samples above the water surface. Results are presented in Table 1, in the V_{above} column.

Based on the detected material type, the densities presented in Section 2.5 were assigned to each sample. Using Eq. (6) and considering measured volume above the water surface (V_{above}) and the assigned densities, the sample volume could be calculated. The calculation results are presented in Table 1, in column V_{cal} .

Additionally, V_{cal} was compared with the actual (pre-determined) volume (V_{act}). Volume errors, expressed as a difference between the actual and the calculated sample volumes are also given in Table 1, both in liters and %.

Further on, we analyzed the impact of floating objects' material type, shape, and orientation on estimated volume errors (in %). Please note that for this analysis, plastic bottles were assigned a cylinder shape. The results are presented in Fig. 9. The median error value for all floating samples is 2.04%, while 50% of cases fall within the range of -7.82 to 9.50%. Regarding the material type results, the maximum dispersion of errors is observed in the case of wooden samples, and the minimum in the case of XPS samples, which probably has to do with the number of cases falling under each category (35 cases were classified as wood and only six as XPS). Also, for the samples made of metal, the proposed method exerts a tendency towards volume overestimation (the median error value is 11.34%). The reason may lie in two plastic samples being incorrectly classified as metal, thus hindering the volume calculation results. Sample orientation has no significant impact on estimated errors, at least when looking at the median values of the error. Regarding shapes, the maximum dispersion of errors is observed in the case of cylindrical shapes. Again, this may be since most of the samples were cylindrical (as already mentioned, bottles were also assigned a cylindrical shape).

As the range of errors was the largest when considering samples made of wood, we decided to perform additional analysis on wood

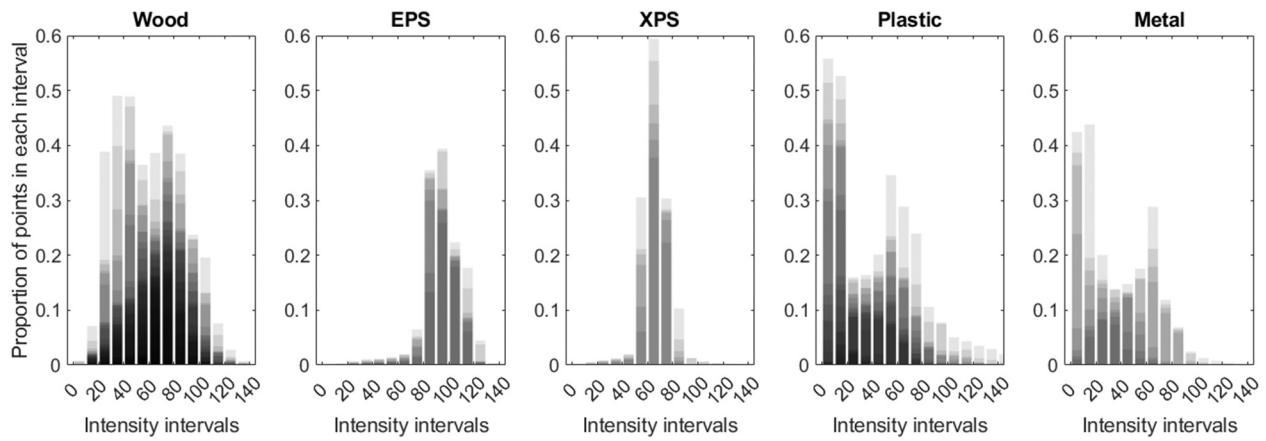


Fig. 6. Intensity footprints for the samples made of different materials.

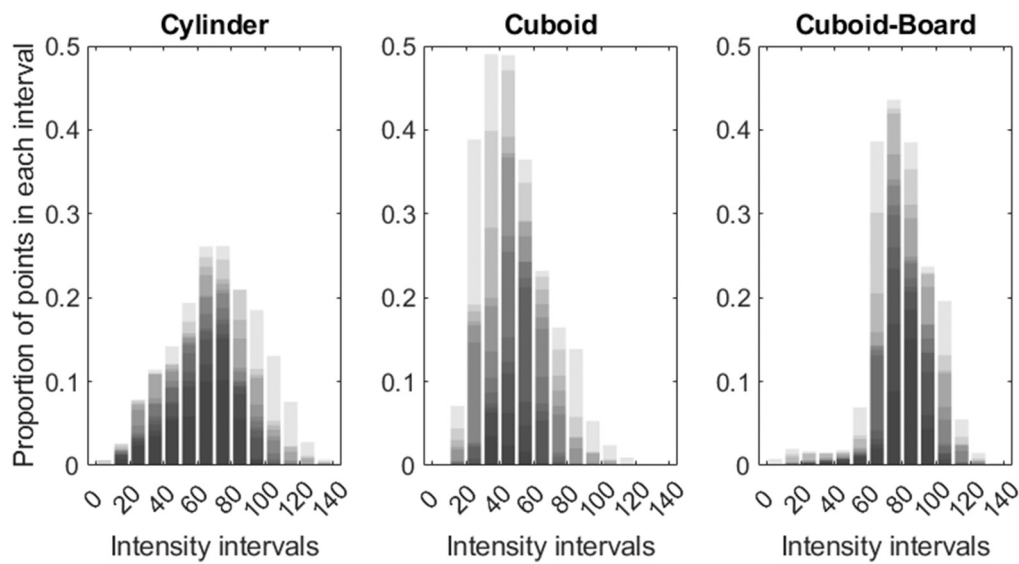


Fig. 7. Intensity footprints for different shapes of wood.

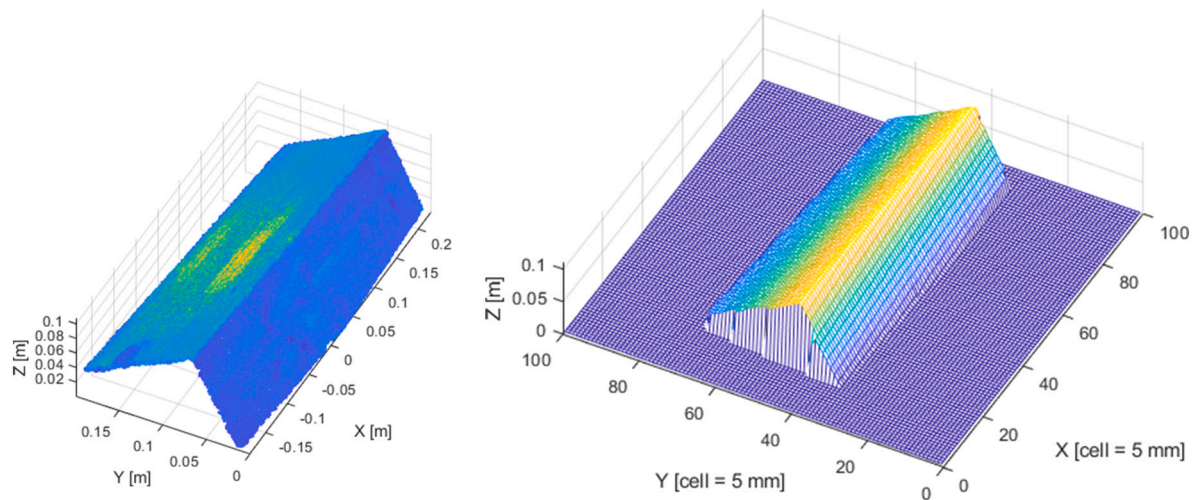


Fig. 8. Filtered point cloud (left) and a mesh (right) for case 15.

Table 1
Volume calculation results.

| Case ID | Sample ID | Material (actual) | Material (detected) | Shape | Orientation | V _{act} [l] | V _{above} [l] | Density [g/l] | V _{cal} [l] | Error [l] | Error [%] |
|---------|-----------|-------------------|---------------------|-----------------------|--------------|----------------------|------------------------|---------------|----------------------|-----------|-----------|
| 1 | 1 | Wood | Wood | Cylinder | Transverse | 2.66 | 0.96 | 580 | 2.29 | -0.37 | -14.04 |
| 2 | 1 | Wood | Wood | Cylinder | Oblique | 2.66 | 0.9 | 580 | 2.14 | -0.52 | -19.41 |
| 3 | 1 | Wood | Wood | Cylinder | Longitudinal | 2.66 | 0.89 | 580 | 2.12 | -0.54 | -20.31 |
| 4 | 2 | Wood | Wood | Cylinder | Longitudinal | 1.91 | 0.74 | 580 | 1.76 | -0.15 | -7.82 |
| 5 | 2 | Wood | Wood | Cylinder | Transverse | 1.91 | 0.85 | 580 | 2.02 | 0.11 | 5.88 |
| 6 | 3 | Wood | Wood | Cylinder | Longitudinal | 0.61 | 0.21 | 580 | 0.50 | -0.11 | -17.79 |
| 7 | 3 | Wood | Wood | Cylinder | Rotating | 0.61 | 0.23 | 580 | 0.55 | -0.06 | -9.96 |
| 8 | 4 | Wood | Wood | Cylinder | Rotating | 0.82 | 0.3 | 580 | 0.71 | -0.10 | -12.59 |
| 9 | 4 | Wood | Wood | Cylinder | Longitudinal | 0.82 | 0.28 | 580 | 0.67 | -0.15 | -18.41 |
| 10 | 4 | Wood | Wood | Cylinder | Transverse | 0.82 | 0.31 | 580 | 0.74 | -0.08 | -9.67 |
| 11 | 5 | Wood | Wood | Cylinder | Longitudinal | 5.98 | 2.89 | 580 | 6.88 | 0.90 | 15.01 |
| 12 | 5 | Wood | Wood | Cylinder | Transverse | 5.98 | 2.76 | 580 | 6.57 | 0.59 | 9.84 |
| 13 | 6 | Wood | Wood | Cuboid | Longitudinal | 8.96 | 4.84 | 580 | 11.52 | 2.56 | 28.61 |
| 14 | 6 | Wood | Wood | Cuboid | Transverse | 8.96 | 4.42 | 580 | 10.52 | 1.56 | 17.45 |
| 15 | 6 | Wood | Wood | Cuboid | Transverse | 8.96 | 4.01 | 580 | 9.55 | 0.59 | 6.56 |
| 16 | 6 | Wood | Wood | Cuboid | Rotating | 8.96 | 4.72 | 580 | 11.24 | 2.28 | 25.43 |
| 17 | 7 | Wood | Wood | Cuboid | Longitudinal | 3.65 | 1.65 | 580 | 3.93 | 0.28 | 7.69 |
| 18 | 7 | Wood | Wood | Cuboid | Transverse | 3.65 | 1.49 | 580 | 3.55 | -0.10 | -2.75 |
| 19 | 8 | Wood | Wood | Cuboid - board | Longitudinal | 1.31 | 0.56 | 580 | 1.33 | 0.03 | 2.12 |
| 20 | 8 | Wood | Wood | Cuboid - board | Transverse | 1.31 | 0.56 | 580 | 1.33 | 0.03 | 2.12 |
| 21 | 9 | Wood | Wood | Cuboid - board | Longitudinal | 1.94 | 0.72 | 580 | 1.71 | -0.23 | -11.85 |
| 22 | 9 | Wood | Wood | Cuboid - board | Transverse | 1.94 | 0.7 | 580 | 1.67 | -0.28 | -14.30 |
| 23 | 10 | Wood | Wood | Cuboid | Rotating | 1.17 | 0.5 | 580 | 1.19 | 0.02 | 2.06 |
| 24 | 10 | Wood | Wood | Cuboid | Transverse | 1.17 | 0.46 | 580 | 1.10 | -0.07 | -6.10 |
| 25 | 11 | Wood | Wood | Cuboid | Longitudinal | 0.90 | 0.39 | 580 | 0.93 | 0.03 | 2.90 |
| 26 | 11 | Wood | Wood | Cuboid | Transverse | 0.90 | 0.31 | 580 | 0.74 | -0.16 | -18.21 |
| 27 | 12 | Wood | Wood | Cuboid | Longitudinal | 2.56 | 1.09 | 580 | 2.60 | 0.04 | 1.38 |
| 28 | 12 | Wood | Wood | Cuboid | Transverse | 2.56 | 1.05 | 580 | 2.50 | -0.06 | -2.34 |
| 29 | 13 | Wood | Wood | Cuboid - board | Longitudinal | 0.60 | 0.27 | 580 | 0.64 | 0.04 | 7.43 |
| 30 | 13 | Wood | Wood | Cuboid - board | Transverse | 0.60 | 0.27 | 580 | 0.64 | 0.04 | 7.43 |
| 31 | 14 | Wood | Wood | Cuboid - board | Longitudinal | 1.22 | 0.55 | 580 | 1.31 | 0.09 | 6.99 |
| 32 | 14 | Wood | Wood | Cuboid - board | Transverse | 1.22 | 0.54 | 580 | 1.29 | 0.06 | 5.04 |
| 33 | 15 | Wood | Wood | Cuboid - board | Longitudinal | 0.67 | 0.34 | 580 | 0.81 | 0.14 | 21.48 |
| 34 | 15 | Wood | Wood | Cuboid - board | Transverse | 0.67 | 0.32 | 580 | 0.76 | 0.10 | 14.33 |
| 35 | 16 | Wood | EPS | Cuboid - board | Longitudinal | 1.93 | 0.92 | 10 | 0.93 | -1.00 | -51.78 |
| 36 | 16 | Wood | Wood | Cuboid - board | Transverse | 1.93 | 1.09 | 580 | 2.60 | 0.67 | 34.66 |
| 37 | 17 | XPS | XPS | Cuboid - board | Longitudinal | 1.10 | 1.16 | 30 | 1.20 | 0.10 | 8.86 |
| 38 | 17 | XPS | XPS | Cuboid - board | Transverse | 1.10 | 1.13 | 30 | 1.16 | 0.07 | 6.05 |
| 39 | 18 | XPS | XPS | Cuboid - board | Longitudinal | 1.94 | 2.06 | 30 | 2.12 | 0.19 | 9.58 |
| 40 | 18 | XPS | XPS | Cuboid - board | Transverse | 1.94 | 2.07 | 30 | 2.13 | 0.20 | 10.11 |
| 41 | 19 | XPS | XPS | Cuboid - board | Longitudinal | 1.71 | 1.65 | 30 | 1.70 | -0.01 | -0.59 |
| 42 | 19 | XPS | Plastic | Cuboid - board | Rotating | 1.71 | 1.65 | 55 | 1.75 | 0.03 | 2.04 |
| 43 | 20 | EPS | EPS | Cuboid - board | Longitudinal | 1.41 | 1.27 | 10 | 1.28 | -0.13 | -9.02 |
| 44 | 20 | EPS | EPS | Cuboid - board | Transverse | 1.41 | 1.53 | 10 | 1.55 | 0.14 | 9.61 |
| 45 | 21 | EPS | EPS | Cuboid - board | Rotating | 1.08 | 1.25 | 10 | 1.26 | 0.19 | 17.38 |
| 46 | 21 | EPS | EPS | Cuboid - board | Transverse | 1.08 | 1.08 | 10 | 1.09 | 0.02 | 1.42 |
| 47 | 22 | EPS | EPS | Cuboid - board | Rotating | 2.56 | 2.41 | 10 | 2.43 | -0.13 | -4.93 |
| 48 | 22 | EPS | EPS | Cuboid - board | Transverse | 2.56 | 2.13 | 10 | 2.15 | -0.41 | -15.98 |
| 49 | 23 | EPS | EPS | Cuboid - board | Longitudinal | 3.61 | 3.39 | 10 | 3.42 | -0.18 | -5.08 |
| 50 | 23 | EPS | EPS | Cuboid - board | Rotating | 3.61 | 3.77 | 10 | 3.81 | 0.20 | 5.56 |
| 51 | 33 | Plastic | Plastic | Container | Longitudinal | 0.86 | 0.78 | 55 | 0.83 | -0.04 | -4.26 |
| 52 | 33 | Plastic | Plastic | Container | Oblique | 0.86 | 0.7 | 55 | 0.74 | -0.12 | -14.08 |
| 53 | 33 | Plastic | Metal | Container | Rotating | 0.86 | 0.99 | 170 | 1.19 | 0.33 | 38.36 |
| 54 | 28 | Metal | Metal | Can with lid | Rotating | 0.28 | 0.22 | 170 | 0.27 | -0.02 | -6.57 |
| 55 | 28 | Metal | Metal | Can with lid | Longitudinal | 0.28 | 0.22 | 170 | 0.27 | -0.02 | -6.57 |
| 56 | 29 | Metal | Wood | Bottle 0.5 l | Oblique | 0.59 | 0.48 | 580 | 1.14 | 0.55 | 93.70 |
| 57 | 29 | Metal | Metal | Bottle 0.5 l | Longitudinal | 0.53 | 0.48 | 170 | 0.58 | 0.05 | 8.78 |
| 58 | 27 | Plastic | Plastic | Wrinkled bottle | Rotating | 1.80 | 1.67 | 55 | 1.77 | -0.03 | -1.60 |
| 59 | 27 | Plastic | Plastic | Wrinkled bottle | Oblique | 1.80 | 1.59 | 55 | 1.68 | -0.11 | -6.32 |
| 60 | 30 | Metal | Metal | Bottle 1 l | Longitudinal | 1.17 | 1.12 | 170 | 1.35 | 0.18 | 14.91 |
| 61 | 30 | Metal | Plastic | Bottle 1 l | Transverse | 1.17 | 1.01 | 55 | 1.07 | -0.11 | -8.98 |
| 62 | 36 | Plastic | Plastic | Bottle with dispenser | Rotating | 0.55 | 0.56 | 55 | 0.59 | 0.05 | 8.69 |
| 63 | 36 | Plastic | Plastic | Bottle with dispenser | Transverse | 0.55 | 0.57 | 55 | 0.60 | 0.06 | 10.63 |
| 64 | 25 | Plastic | Plastic | Bottle | Longitudinal | 1.15 | 1.12 | 55 | 1.19 | 0.04 | 3.42 |
| 65 | 25 | Plastic | Plastic | Bottle | Transverse | 1.15 | 1.02 | 55 | 1.08 | -0.07 | -5.81 |
| 66 | 24 | Plastic | Plastic | Bottle with dispenser | Longitudinal | 1.15 | 1.06 | 55 | 1.12 | -0.02 | -2.12 |
| 67 | 24 | Plastic | Plastic | Bottle with dispenser | Transverse | 1.15 | 1.24 | 55 | 1.31 | 0.17 | 14.50 |
| 68 | 26 | Plastic | Plastic | Container | Longitudinal | 1.34 | 0.93 | 55 | 0.98 | -0.36 | -26.72 |
| 69 | 26 | Plastic | Plastic | Container | Transverse | 1.34 | 1.27 | 55 | 1.34 | 0.00 | 0.07 |

(continued on next page)

Table 1 (continued)

| Case ID | Sample ID | Material (actual) | Material (detected) | Shape | Orientation | V _{act} [l] | V _{above} [l] | Density [g/l] | V _{cal} [l] | Error [l] | Error [%] |
|---------|-----------|-------------------|---------------------|---------------|--------------|----------------------|------------------------|---------------|----------------------|-----------|-----------|
| 70 | 32 | Plastic | Plastic | Bottle 0.33 l | Longitudinal | 0.35 | 0.36 | 55 | 0.38 | 0.03 | 7.47 |
| 71 | 32 | Plastic | Plastic | Bottle 0.33 l | Oblique | 0.35 | 0.34 | 55 | 0.36 | 0.01 | 1.50 |
| 72 | 31 | Metal | Metal | Bottle 1 l | Rotating | 1.17 | 1.11 | 170 | 1.34 | 0.16 | 13.89 |
| 73 | 31 | Metal | Metal | Bottle 1 l | Transverse | 1.17 | 0.99 | 170 | 1.19 | 0.02 | 1.58 |
| 74 | 35 | Plastic | Plastic | Bottle 10 l | Longitudinal | 12.29 | 8.22 | 55 | 8.70 | -3.59 | -29.24 |
| 75 | 35 | Plastic | Plastic | Bottle 10 l | Transverse | 12.29 | 12.72 | 55 | 13.46 | 1.17 | 9.50 |
| 76 | 34 | Plastic | XPS | Cup with lid | Down | 0.65 | 0.51 | 30 | 0.53 | -0.12 | -19.11 |
| 77 | 34 | Plastic | Metal | Cup with lid | Up | 0.65 | 0.68 | 170 | 0.82 | 0.17 | 26.04 |

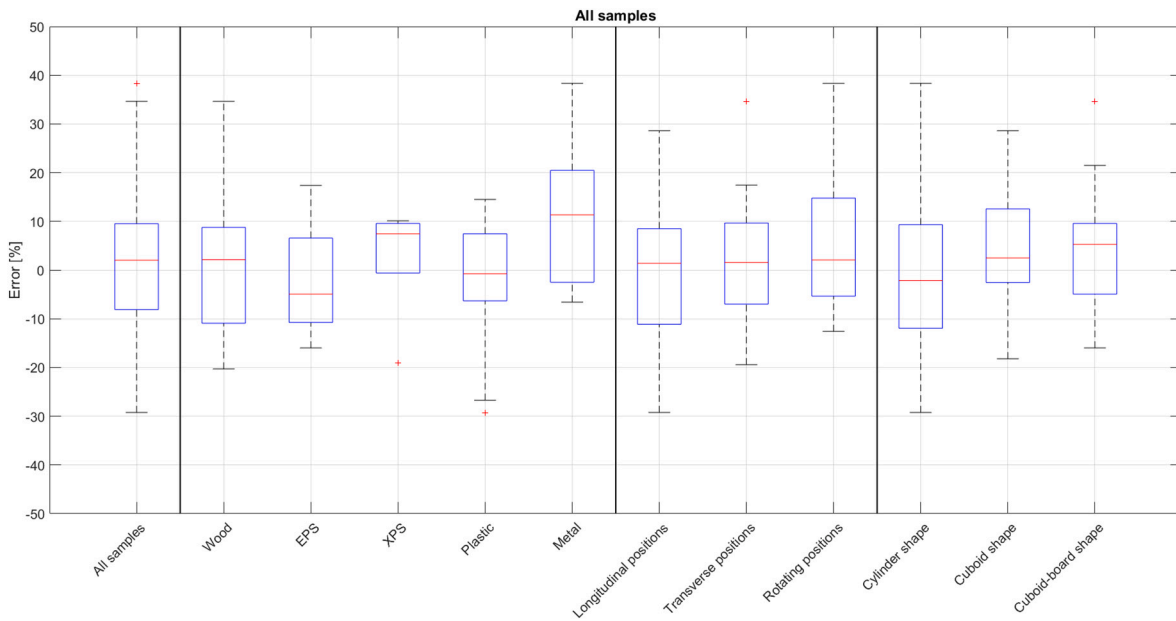


Fig. 9. Impact of material type, orientation and shape on volume errors.

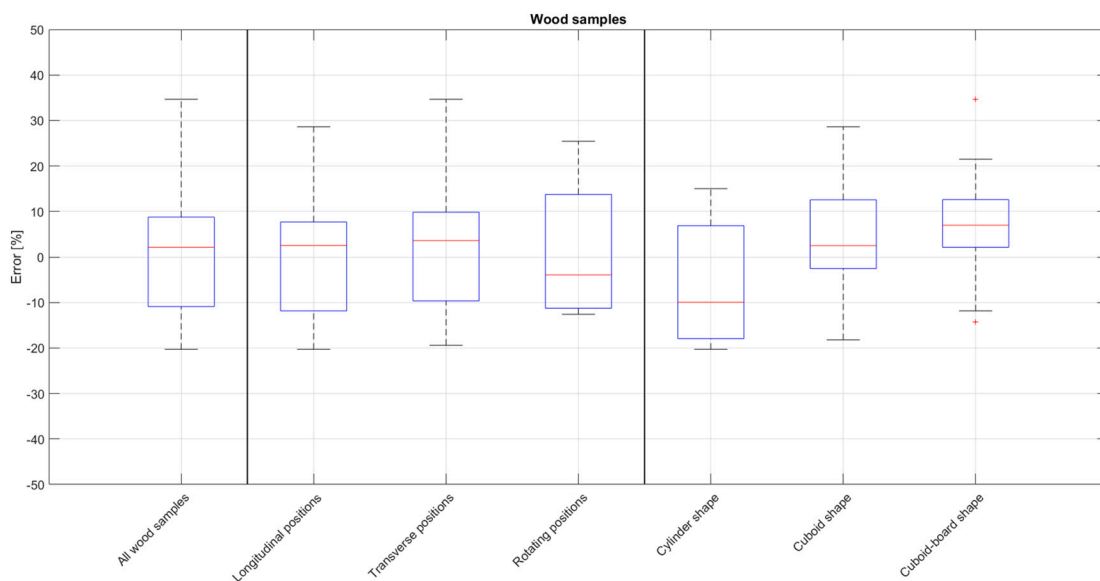


Fig. 10. Wood samples: impact of shape and orientation on volume errors.

samples only. These results are presented in Fig. 10. The median error value for all wood samples is 2.12%, while 50% of cases fall within the range of -10.44 to 8.23% . The volumes of rotating and cylinder-shaped samples are slightly underestimated compared to the floating objects of other orientations and shapes.

4. Discussion

4.1. Material misclassification and volume errors

Volume errors are mostly related to material misclassification. For example, in case 56, the floating sample made of metal was classified as wood. Thus, it was assigned a higher density (580 g/l instead of 170 g/l). Consequently, the calculated volume was significantly overestimated (i. e., by 93.7%).

Most of the misclassifications (i. e., cases 35, 42, 56, and 61) are hard to interpret. The histograms of the misclassified cases must have been similar to ones typical for other materials. For example, the histogram for case 53 (rotating sample 33, i. e., plastic container coated with a thin layer of glossy black foil) must have been similar to the histograms of metal samples, which could be due to its smooth covering. Also, cases 76 and 77, corresponding to sample 34 (i. e., the only plastic container facing the scanner with its flat surface) were not correctly classified. As this container was very different from the other plastic samples, the machine learning algorithm could not differentiate it successfully. To improve the classification, more various samples would be needed so that the algorithm could learn from them.

In general, histograms for different material types look different because of the remission, i. e., the ability of a material to reflect light. According to Lambert-Beer law, the remission value of an object correlates with the ratio of the laser light amount emitted by the LIDAR sensor falling on the object and the amount reflected by the object. Thus, the reflection intensities are affected by the material type and shape, namely by the incident of a laser beam. Shiny surfaces tend to have different remission values at different angles of incidence, while matt and dull surfaces have a diffuse remission and, consequently, similar relative remission values independent of the incidence angle (SICK, 2020).

The main focus of our research was on the automatic identification of the floating object's material type to enable the correct assignment of its density. Since only one wooden object case (i. e., case 35) was incorrectly classified as the EPS, we believe this task was successful, regardless of the identified shape impact, seen in Fig. 7.

Additionally, two scanning problems were identified that might cause volume errors. The first one is related to scanning shadows. In some cases, the orientation of the floating object may prevent the laser scanner from scanning its entire above-water surface, i. e., it may be casting a shadow. Examples of scanning shadows are presented in Fig. 11. In such cases, only a visible part of the object is scanned. The volume is computed for the vertical projection of the visible surface, as explained in Section 2.3.

The second one is related to the rotation of the floating objects. While rotating, one part of the object flows faster than the other related to the scanner. That is why the average velocity of a sample perpendicular to the scanning sheet determined with post-processing of image sequences can be underestimated. Thus, the faster side of the object is detected as shorter and the slower as longer (Fig. 12), which may cause errors in volume calculation.

However, the results, presented in Fig. 9, show that the average volume errors of rotating objects do not differ from the errors obtained for the non-rotating samples, while the volumes of rotating wood objects are only slightly underestimated compared to other orientations (Fig. 10).

Reynolds number and free-surface water velocity (i. e., $3.3 \cdot 10^4$ and 0.16 m/s, respectively) used within the presented research are comparable with the values for the middle and lower river courses but lower than the values for the upper natural river courses or during high water

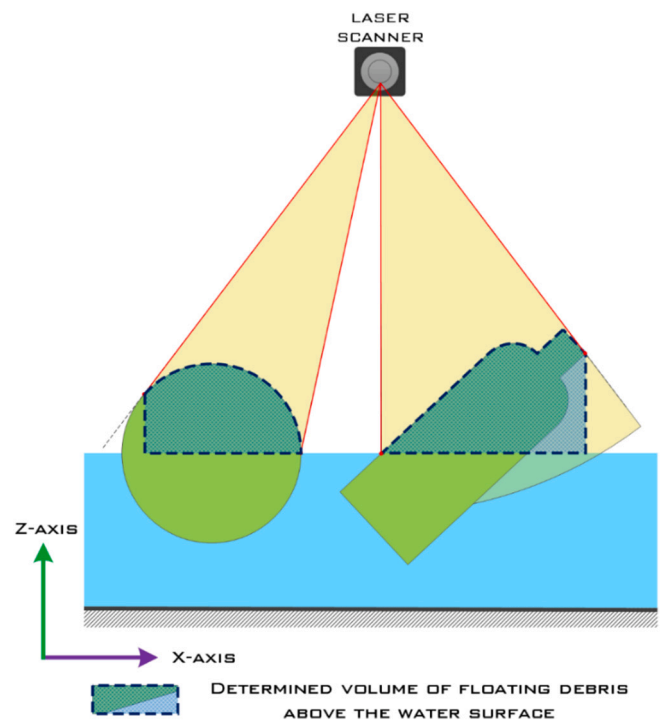


Fig. 11. Scanning shadows.

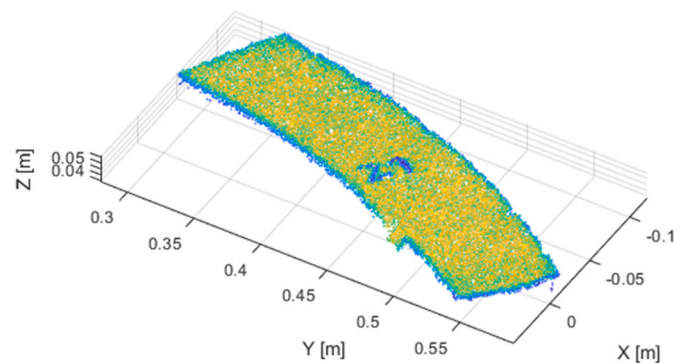


Fig. 12. Point cloud of a rotating sample (case 45, sample 21).

events. However, due to the high sampling rate of the fast camera and LIDAR, higher water flow velocities should not affect the data acquisition capability. More than a flow regime, an undulated or rough free-water surface could cause tossing and consequently misinterpretation of a floating object and false estimation of its immersed part when crossing the measuring section, which could also lead to incorrect assessment of the volumes of floating objects.

4.2. Recommendations for practical application

Testing laser scanner for water level acquisition in case of relatively smooth water surface revealed relatively high measurement uncertainty (up to 10 cm), significant noise, and poor usability in cases of clear water (Rak et al., 2017). While such an error might be acceptable in real-world applications, it is unacceptable in laboratory experiments. That is why we used the ultrasonic sensor for water level detection. However, for the practical application, the ultrasonic sensor could be removed since water is rarely entirely clear and as it contains suspended particles from which the laser beam could be reflected, but also because the measurement uncertainty is less significant for the field measurements. Still, one camera would be needed to determine the velocity of objects

relative to the laser sheet to transform raw LIDAR point cloud along the axis perpendicular to the laser sheet and, consequently, estimate the shape and volume of objects above the water surface.

The width part of the channel covered with one laser scanner depends on its installation height. In general, laser scanners' field of view ranges from 70° to 270° with different angular resolutions. However, increasing the incidence angle on the water surface can result in scanning shadows presented in Fig. 11. These could be eliminated by using two overlapping LIDAR sensors. In the case of wider rivers, more laser scanners would be needed. As such laser scanners are widely used for continuous measurements in industry, they have low energy consumption.

In real-world applications, the densities of the floating objects are not provided and have to be somehow estimated. In the proposed method, material recognition based on laser scanning measurements and machine learning is used for this purpose. For the identified wood objects, density estimations could rely on the most common (dominant) wood species in the contributing catchment and recommendations from the literature. For example, Ruiz-Villanueva et al. (2016b) provide a range of $660 \pm 200 \text{ kg/m}^3$ for in-channel wood belonging to broad-leaved tree species. Additionally, the densities could be adapted to particular flood conditions, e.g., average flood events might result in mostly fresh in-channel wood, while during more intense flood events, in-channel wood could also consist of drier (older) wood already exhibiting signs of decay. For the EPS and XPS samples, the average values provided by the manufacturers could be used, i.e., 10 kg/m^3 and 30 kg/m^3 , respectively.

Recent studies on riverine plastic pollution (van Emmerik and Schwarz, 2020; Al-Zawaidah et al., 2021) have revealed its diverse range of sizes (i.e., nano-, micro-, and macroplastics), forms (i.e., fibers, films, and solid pieces), and densities (e.g., from 910 to 2300 kg/m^3 for plastic polymers). Since we only tested empty plastic objects, the density values of raw material could not be applied directly. Namely, an empty volume or volume filled with unknown content can affect the density of a floating object even more than the plastic object's type. Therefore, the assignment of densities to the identified plastic and metal objects remains problematic, as, in the real world, it is not possible to determine whether a floating packaging object (either metal or plastic) is empty or full. However, assuming that most waste packaging is (almost) empty, the average densities obtained in the laboratory (based on testing various types of containers) should be attributed separately for plastic and metal products, for which the proposed values are 55 kg/m^3 and 170 kg/m^3 , respectively. However, these values might change after examining more packaging samples, which is foreseen in the future.

4.3. Comparison with the other methods

Stereo-vision acquisition of floating objects might outperform the proposed method in the case of rotating objects as camera shots are executed in a moment. While using LIDAR, one part of the rotating object flows faster than the other related to the scanner. Thus, the velocity of a sample perpendicular to the scanning sheet determined with post-processing of image sequences could be underestimated. Consequently, the faster side of the object is detected as shorter and the slower as longer, which may cause errors in volume calculation. Anyway, the results show that the volumes of rotating samples are just slightly underestimated compared to the measurements of the same, non-rotating objects.

Compared to the proposed approach, stereo-vision and SfM are more sensitive to water surface topography and turbulence. Another notable advantage of our method is that it needs very little light, only to detect particles on the water surface, based on which water velocity may be determined, while it is not required for objects' detection by the LIDAR sensor. Thus, it could also be used during the night, without any additional light source (the street lights on the bridges would probably suffice). Also, the proposed method allows for a very detailed estimation of

the volume above the water surface using a single static scanner, while the application of stereo-vision requires at least two cameras. On the other hand, SfM could be applied using a single camera but requires changing its position and orientation. So far, the SfM has been used for the volume estimation of the static piles of in-channel wood. Thus, the question is how it would perform in the case of moving objects.

5. Conclusions

The paper presents a non-intrusive measuring method for the acquisition of floating objects in an open channel. The proposed methodology was tested in the straight rectangular flume. Results of the research show that laser scanning in combination with a high-speed camera and ultrasonic sensor can provide raw data, which enables further post-processing and qualitative, as well as quantitative analysis of the floating elements. Due to the laser beam reflections from the water surface, laser scanning can only detect a part of the floating object above the water surface. Thus, to calculate its entire volume, the appropriate material-dependent density has to be assigned. To this end, the histogram analysis of the laser beam intensities reflected from the sample's surface was performed using the IBk machine learning algorithm, which revealed that different types of material have distinct fingerprints.

Based on the automatic material type identification and the assigned density, the floating sample volume could be calculated and compared with the pre-determined (actual) one. The results reveal that the volume error is approximately 2% on average. Mostly, it is affected by material type identification, and to a lesser extent, by sample orientation and shape.

The presented method proved fast, reliable, and relatively robust. It requires already installed measuring equipment at river monitoring gauges with a few additional, not very expensive, and operationally undemanding devices. Besides the advantages, the method limitations are presented concerning the material type misclassifications, scanning shadows, and problems encountered while scanning the rotating samples.

At this first stage of the experiment, we have only conducted measurements with individual samples under controlled laboratory conditions. Since we are introducing a new method for the acquisition of in-channel wood and other floating objects of various material types, our goal was to investigate the applicability of the proposed method and its capability of object identification, material recognition, and volume estimation.

Next, we will perform laboratory measurements using multiple objects, either of the same or different materials. We expect that in the case of samples having no contact when passing the laser scanner, the proposed approach should give equally reliable results as presented in this research, even if the objects are made of different materials. On the other hand, clusters of samples of different characteristics could affect material recognition and, consequently, the process of assigning the densities and misestimation of objects' volumes.

After solving all the potential issues arising during laboratory measurements, we would like to test the proposed approach in a real-world application.

In natural rivers and streams, especially in their upper/torrential parts, in-channel wood is usually the prevailing floating object type affecting ecological processes, causing obstruction problems, and increasing flood hazard potential. Thus, further work will focus on testing the proposed methodology on wood logs of different tree species. Additionally, more plastic and metal samples of various shapes will be tested to improve the material recognition process.

Declaration of competing interest

The authors declare that they have no known competing financial interests or personal relationships that could have appeared to influence the work reported in this paper.

Acknowledgements

The authors acknowledge the financial support from the Slovenian

Research Agency (research core funding No. P2-0180 and P2-0227).

Appendix A. 10-Fold cross-validation results (IBk, $k = 1$)

Summary

| | |
|----------------------------------|---------------|
| Correctly classified instances | 70 (90.9091%) |
| Incorrectly classified instances | 7 (9.0909%) |
| Kappa statistic | 0.8691 |
| Mean absolute error | 0.0555 |
| Root mean squared error | 0.1861 |
| Relative absolute error | 19.7631% |
| Root relative squared error | 49.874% |
| Total number of instances | 77 |

Detailed accuracy by class

| | TP rate | FP rate | Precision | Recall | F-measure | MCC | ROC area | PRC area | Class |
|---------------|---------|---------|-----------|--------|-----------|-------|----------|----------|---------|
| | 0.972 | 0.024 | 0.972 | 0.972 | 0.972 | 0.948 | 0.981 | 0.968 | Wood |
| | 0.842 | 0.034 | 0.889 | 0.842 | 0.865 | 0.823 | 0.921 | 0.786 | Plastic |
| | 0.750 | 0.029 | 0.750 | 0.750 | 0.750 | 0.721 | 0.899 | 0.659 | Metal |
| | 0.833 | 0.014 | 0.833 | 0.833 | 0.833 | 0.819 | 0.851 | 0.763 | XPS |
| | 1.000 | 0.014 | 0.889 | 1.000 | 0.941 | 0.936 | 0.994 | 0.903 | EPS |
| Weighted avg. | 0.909 | 0.026 | 0.909 | 0.909 | 0.909 | 0.882 | 0.949 | 0.868 | |

Confusion matrix

| | a | b | c | d | e | ← classified as |
|----|----|---|---|---|---|-----------------|
| 35 | 0 | 0 | 0 | 0 | 1 | a = wood |
| 0 | 16 | 2 | 1 | 1 | 0 | b = plastic |
| 1 | 1 | 6 | 0 | 0 | 0 | c = metal |
| 0 | 1 | 0 | 5 | 0 | 0 | d = XPS |
| 0 | 0 | 0 | 0 | 0 | 8 | e = EPS |

References

- Abalharth, M., Hassan, M., Klinkenberg, B., Leung, V., McCleary, R., 2015. Using LiDAR to characterize logjams in lowland rivers. *Geomorphology* 246, 531–541. <https://doi.org/10.1016/j.geomorph.2015.06.036>.
- Aha, D.W., Kibler, D., Albert, M.K., 1991. *Instance-based learning algorithms*. *Mach. Learn.* 6, 37–66.
- Al-Zawaidah, H., Ravazzolo, D., Friedrich, H., 2021. Macroplastics in rivers: present knowledge, issues and challenges. *Environ. Sci. - Proc. Imp.* 23, 535–552. <https://doi.org/10.1039/d0em00517g>.
- Atha, J., 2013. Identification of fluvial wood using Google Earth. *River Res. Appl.* 30, 857–864. <https://doi.org/10.1002/rra.2683>.
- Atha, J.B., Dietrich, J.T., 2016. Detecting fluvial wood in forested watersheds using LiDAR data: a methodological assessment. *River Res. Appl.* 32, 1587–1596. <https://doi.org/10.1002/rra.2989>.
- Bajcar, T., Širok, B., Eberlinc, M., 2009. Quantification of flow kinematics using computer-aided visualization. *Stroj. Vestn.-J. Mech. E* 55, 215–223.
- Bizjan, B., Orbanic, A., Širok, B., Kovač, B., Bajcar, T., Kavkler, I., 2014. A computer-aided visualization method for flow analysis. *Flow Meas. Instrum.* 38, 1–8. <https://doi.org/10.1016/j.flowmeasinst.2014.05.017>.
- Bung, D.B., Valero, D., 2016. Optical flow estimation in aerated flows. *J. Hydraul. Res.* 54, 575–580. <https://doi.org/10.1080/00221686.2016.1173600>.
- Comiti, F., Lucía, A., Rickenmann, D., 2016. Large wood recruitment and transport during largefloods: a review. *Geomorphology* 269, 23–39. <https://doi.org/10.1016/j.geomorph.2016.06.016>.
- Fan, L., McGrath, D., Chong, C.T., Jaafar, M.N., Zhong, H., Hochgreb, S., 2018. Laser-induced incandescence particle image velocimetry (LII-PIV) for two-phase flow velocity measurement. *Exp. Fluids* 59, 156. <https://doi.org/10.1007/s00348-018-2610-4>.
- Ghaffarian, H., Piégay, H., Lopez, D., Rivière, N., MacVicar, B., Antonio, A., Mignot, E., 2020a. Video-monitoring of wood discharge: first inter-basin comparison and recommendations to install video cameras. *Earth Surf. Proc. Landf.* 45, 2219–2234. <https://doi.org/10.1002/esp.4875>.
- Ghaffarian, H., Lopez, D., Mignot, E., Piégay, H., Rivière, N., 2020b. Dynamics of floating objects at high particulate Reynolds numbers. *Phys. Rev. Fluids.* 5, 054307. <https://doi.org/10.1103/PhysRevFluids.5.054307>.
- Ghaffarian, H., Lemaire, P., Zhi, Z., Tougne, L., MacVicar, B., Piégay, H., 2021. Automated quantification of floating wood pieces in rivers from video monitoring: a new software tool and validation. *Earth Surf. Dyn.* 9, 519–537. <https://doi.org/10.5194/esurf-9-519-2021>.
- Grigillo, D., Vrečko, A., Mikoš, M., Gvozdanović, T., Anžur, A., Vezočnik, R., Petrovič, D., 2015. Determination of large wood accumulation in a steep forested torrent using laser scanning. In: Lollino, G., Arattano, M., Rinaldi, M., Giustolisi, O., Marechal, J. C., Grant, G.E. (Eds.), *Engineering Geology for Society and Territory – Volume 3: River Basins, Reservoir Sedimentation and Water Resources*. Springer, Cham, pp. 127–130. https://doi.org/10.1007/978-3-319-09054-2_24.
- Gschntzer, T., Gerns, B., Mazzorana, B., Aufleger, M., 2017. Towards a robust assessment of bridge clogging processes in flood risk management. *Geomorphology* 279, 128–140. <https://doi.org/10.1016/j.geomorph.2016.11.002>.
- Hu, C., 2021. Remote detection of marine debris using satellite observations in the visible and near infrared spectral range: challenges and potentials. *Remote Sens. Environ.* 259, 112414. <https://doi.org/10.1016/j.rse.2021.112414>.
- Kantoush, S.A., De Cesare, G., Boillat, J.L., Schleiss, A.J., 2008. Flow field investigation in a rectangular shallow reservoir using UVP, LSPIV and numerical modelling. *Flow Meas. Instrum.* 19, 139–144. <https://doi.org/10.1016/j.flowmeasinst.2007.09.005>.
- Kasprak, A., Magilligan, F.J., Nislow, K.H., Snyder, N.P., 2012. A Lidar-derived evaluation of watershed-scale large woody debris sources and recruitment mechanisms: coastal Maine, USA. *River Res. Applic.* 28, 1462–1476. <https://doi.org/10.1002/rra.1532>.
- Khosravi, K., Cooper, J.R., Daggupati, P., Thai Pham, B., Tien Bui, D., 2020. Bedload transport rate prediction: application of novel hybrid data mining techniques. *J. Hydrol.* 585, 124774. <https://doi.org/10.1016/j.jhydrol.2020.124774>.

- Khosravi, K., Khozani, Z.S., Cooper, J.R., 2021. Predicting stable gravel-bed river hydraulic geometry: a test of novel, advanced, hybrid data mining algorithms. *Environ. Model. Softw.* 144, 105165 <https://doi.org/10.1016/j.envsoft.2021.105165>.
- Kramer, N., Wohl, E., 2015. Driftcretions: the legacy impacts of driftwood on shoreline morphology. *Geophys. Res. Lett.* 42, 5855–5864. <https://doi.org/10.1002/2015GL064441>.
- Kramer, M., Chanson, H., Felder, S., 2020. Can we improve the non-intrusive characterization of high-velocity air–water flows? Application of LIDAR technology to stepped spillways. *J. Hydraul. Res.* 58, 350–362. <https://doi.org/10.1080/00221686.2019.1581670>.
- MacVicar, B.J., Piégay, H., 2012. Implementation and validation of video monitoring for wood budgeting in a wandering Piedmont river, the Ain River (France). *Earth Surf. Proc. Landf.* 37, 1272–1289. <https://doi.org/10.1002/esp.3240>.
- Magnussen, S., Nord-Larsen, T., Riis-Nielsen, T., 2018. Lidar supported estimators of wood volume and aboveground biomass from the danish national forest inventory (2012–2016). *Remote Sens. Environ.* 211, 146–153. <https://doi.org/10.1016/j.rse.2018.04.015>.
- Montano, L., Felder, S., 2018. LIDAR measurements of free-surface profiles and turbulent scales in a hydraulic jump. In: Bung, D., Tullis, B. (Eds.), 7th IAHR International Symposium on Hydraulic Structures (ISHS), Aachen, Germany, 15–18 May 2018. <https://doi.org/10.15142/T3Q64F>.
- Mosavi, A., Ozturk, P., Kwok-wing, C., 2018. Flood prediction using machine learning models: literature review. *Water* 10, 1536. <https://doi.org/10.3390/w10111536>.
- Müller, M., Novak, G., Steinman, F., Rak, G., Bajcar, T., 2015. Influence of the operating and geometric characteristics of a bottom-hinged flap gate. *J. Mech. Eng.* 61, 498–506. <https://doi.org/10.5545/sv-jme.2015.2453>.
- Novak, G., Rak, G., Prešeren, T., Bajcar, T., 2017. Non-intrusive measurements of shallow water discharge. *Flow Meas. Instrum.* 56, 14–17. <https://doi.org/10.1016/j.flowmeasinst.2017.05.007>.
- Panici, D., Kripakaran, P., Djordjević, S., Dentith, K., 2020. A practical method to assess risks from large wood debris accumulations at bridge piers. *Sci. Total Environ.* 728, 138575 <https://doi.org/10.1016/j.scitotenv.2020.138575>.
- Rak, G., Hočevar, M., Steinman, F., 2017. Measuring water surface topography using laser scanning. *Flow Meas. Instrum.* 56, 35–44. <https://doi.org/10.1016/j.flowmeasinst.2017.07.004>.
- Rak, G., Steinman, F., Hočevar, M., Dular, M., Jezeršek, M., Pavlovčič, U., 2020a. Laser ranging measurements of turbulent water surfaces. *Eur. J. Mech. B-Fluid.* 81, 165–172. <https://doi.org/10.1016/j.euromechflu.2020.02.001>.
- Rak, G., Hočevar, M., Steinman, F., 2020b. Non-intrusive measurements of free-water-surface profiles and fluctuations of turbulent, two-phase flow using 2-D laser scanner. *Meas. Sci. Technol.* 31, 064001 <https://doi.org/10.1088/1361-6501/ab727f>.
- Ruiz-Villanueva, V., Piégay, H., Gurnell, A., Marston, R.A., Stoffel, M., 2016a. Recent advances quantifying the large wood cycle and dynamics in river basins: new methods, remaining challenges. *Rev. Geophys.* 54, 611–652. <https://doi.org/10.1002/2015RG000514>.
- Ruiz-Villanueva, V., Piégay, H., Gaertner, V., Perret, F., Stoffel, M., 2016b. Wood density and moisture sorption and its influence on large wood mobility in rivers. *Catena* 140, 182–194. <https://doi.org/10.1016/j.catena.2016.02.001>.
- Sanhueza, D., Picco, L., Ruiz-Villanueva, V., Iroumé, A., Ulloa, H., Barrientos, G., 2019. Quantification of fluvial wood using UAVs and structure from motion. *Geomorphology* 345, 106837. <https://doi.org/10.1016/j.geomorph.2019.106837>.
- SICK, 2020. LMS4000 2D LiDAR Sensors: Operating Instructions. SICK AG, Waldkirch, Germany.
- Spreitzer, G., Tunnicliffe, J., Friedrich, H., 2019. Using Structure from Motion photogrammetry to assess large wood (LW) accumulations in the field. *Geomorphology* 346, 106851. <https://doi.org/10.1016/j.geomorph.2019.106851>.
- Spreitzer, G., Tunnicliffe, J., Friedrich, H., 2020. Large wood (LW) 3D accumulation mapping and assessment using structure from motion photogrammetry in the laboratory. *J. Hydrol.* 581, 124430 <https://doi.org/10.1016/j.jhydrol.2019.124430>.
- Tonon, A., Picco, L., Ravazzolo, D., Lenzi, M.A., 2014. Using a terrestrial laser scanner to detect wood characteristics in gravel-bed rivers. *J. Agric. Eng. XLV* (431), 161–167. <https://doi.org/10.4081/jae.2014.431>.
- Ulloa, H., Iroumé, A., Mao, L., Andreoli, A., Diez, S., Lara, L.E., 2015. Use of remote imagery to analyse changes in morphology and longitudinal large Wood distribution in the Blanco River after the 2008 Chaitén volcanic eruption, Southern Chile. *Geogr. Ann. Ser. A Phys. Geogr.* 97, 523–541. <https://doi.org/10.1111/geoa.12091>.
- van Emmerik, T., Schwarz, A., 2020. Plastic debris in rivers. *WIREsWater* 7, e1398. <https://doi.org/10.1002/wat2.1398>.
- Wohl, E., Kramer, N., Ruiz-Villanueva, V., Scott, D., Comiti, F., Gurnell, A., Piégay, H., Lininger, K., Jaeger, K., Walters, D., Fausch, K., 2019. The natural wood regime. *Bioscience* 69, 259–273. <https://doi.org/10.1093/biosci/biz013>.
- Zhang, G., Valero, D., Bung, D.B., Chanson, H., 2018. On the estimation of free-surface turbulence using ultrasonic sensors. *Flow Meas. Instrum.* 60, 171–184. <https://doi.org/10.1016/j.flowmeasinst.2018.02.009>.
- Zhang, Z., Ghaffarian, H., Macvicar, B., Vaudor, L., Antonio, A., Michel, K., Piégay, H., 2021. Video monitoring of in-channel wood: from flux characterization and prediction to recommendations to equip stations. *Earth Surf. Proc. Land.* 46, 822–836. <https://doi.org/10.1002/esp.5068>.